Article

Not peer-reviewed version

Fault Location in Distribution Networks Using Apparent Inductance-Based Algorithm

Obed Muhayimana * , Petr Toman , Matti Lehtonen , Ali Aljazaeri , He Li , Silas Tuyishime

Posted Date: 19 May 2026

doi: 10.20944/preprints202605.1201.v1

Keywords: apparent inductance; active distribution networks; distribution systems; distributed energy resources; fault location; fault resistance

Article

Fault Location in Distribution Networks Using Apparent Inductance-Based Algorithm

Obed Muhayimana [1,*], Petr Toman [1], Matti Lehtonen [2], Ali Aljazaeri [1], He Li [2] and Silas Tuyishime [3]

[1] Brno University of Technology, Faculty of Electrical Engineering and Communication, Brno, Czechia
[2] Aalto University, School of Electrical Engineering, Espoo, Finland
[3] University of Rwanda, School of Engineering, Kigali, Rwanda
* Correspondence: xmuhay00@vut.cz; Tel.: +420608388813

Abstract

Accurate fault location is essential for rapid service restoration in distribution networks. However, modern active distribution networks (ADNs) with high penetration of distributed energy resources (DERs) challenge conventional methods through multi-source fault contributions, bidirectional power flows, and converter-limited fault currents. This paper presents a time-domain fault-location method for both passive distribution networks (PDNs) and ADNs, based on a three-sample apparent-inductance estimator that uses local voltage and current measurements. The estimator exploits the strong correlation between line inductance and fault distance, with reduced sensitivity to fault resistance compared to classical impedance approaches. Its performance is evaluated on a 22 kV, 20 km distribution feeder, covering three fault types, four fault resistance levels (5–500 Ω), four fault locations, EN 50160 standard-compliant harmonic distortion, and DER penetration levels from 0 to 80%. Under ideal sinusoidal conditions, relative location errors remain below 2% for low-resistance faults. In ADNs, the method achieves errors below 5% for low-resistance faults across all fault types, with accuracy decreasing for high-resistance faults at high DER penetration. A sensitivity analysis confirms practical robustness across SNR, load current, THD, and DER penetration.

Keywords: apparent inductance; active distribution networks; distribution systems; distributed energy resources; fault location; fault resistance

1. Introduction

Faults in electrical distribution networks are a major cause of power outages and reliability degradation in modern power systems. Recent statistics indicate that around 90% of power system outages result from distribution network disturbances [1]. Rapid and accurate fault location is therefore essential for efficient service restoration and continuous supply quality. The increasing deployment of digital relays, monitoring devices, and synchrophasor technologies has enhanced system observability. However, their application in distribution systems remains challenging due to feeder characteristics such as high resistance-to-reactance (R/X) ratios, unbalanced operation, and variable loading conditions, compounded by the multi-lateral topology of most feeders which introduces multiple parallel current paths that complicate impedance-based measurements [2]. These characteristics significantly limit the effectiveness of classical impedance-based fault location techniques that were originally developed for transmission networks.

These challenges are further reinforced by the ongoing structural transformation of distribution networks driven by the large-scale integration of distributed energy resources (DERs), including photovoltaic systems, wind turbines, battery storage units, and small-scale generators, increasingly connected at the medium- and low-voltage levels [3]. This evolution from traditionally passive distribution networks (PDNs) with unidirectional power flow to active distribution networks (ADNs) with bidirectional flows and intermittent generation improves system flexibility and sustainability,

 doi:10.20944/preprints202605.1201.v1

but also fundamentally alters the fault response. Multi-source fault current contributions, dynamic voltage profiles, and converter-limited fault currents challenge the protection and monitoring schemes that were originally designed for radial feeders [4–6].

Fault location techniques are commonly classified into impedance-based, travelling-wave-based, and data-driven approaches. Traditional single-ended impedance methods are attractive for their simplicity and compatibility with existing infrastructure [4,7], but exhibit poor accuracy in the presence of high fault resistance, waveform distortion, and measurement noise [8]. Time-domain formulations that exploit transient voltage and current information have been proposed to improve robustness [9,10,24], while steady-state matching and distance-metric approaches address complex feeder topologies [11]. More recently, inductance-oriented strategies have been introduced, exploiting the fact that the inductive component of the line impedance remains strongly correlated with distance even when resistive effects and fault resistance introduce significant uncertainty [12]. Travelling-wave methods can achieve high accuracy but require high-bandwidth sensors, precise time synchronisation, and careful handling of wave reflections, limiting their large-scale deployment [13,14,22]. Data-driven approaches based on machine learning and graph-based models offer promising performance but often require extensive training data and raise concerns regarding generalization across different operating conditions [15,16]. Comprehensive reviews and industry standards summarize the advantages and practical limitations of these approaches [17,18].

Despite these advancements, many existing methods require high-frequency sampling, multiple synchronized measurement points, or detailed system models, limiting their applicability in real-world networks [19]. In ADNs specifically, the apparent impedance seen at a single terminal no longer corresponds directly to the physical line segment between the substation and the fault, as inverter-based resources limit and control their fault current output, leading to nontraditional current waveforms [5,6,16,20]. Recent studies have highlighted that protection systems in high-inverter-penetration networks may experience miscoordination, underreaching or overreaching of distance locators, and reduced sensitivity to high-resistance faults [6,20].

The proposed apparent inductance-based fault location method provides a promising alternative in this context. By directly exploiting the inductive relationship between voltage and current, they operate in the time domain, require only local measurements, and can be implemented using a small number of samples, making them well-suited for both passive and active distribution networks. The inductive component of the line impedance remains strongly correlated with distance even under adverse conditions [12]. In ADNs, however, the apparent inductance observed at the substation is also influenced by local DER injections, which may bias the inductance estimation and the inferred fault distance. To date, most studies addressing DER impacts have focused on protection coordination and relay performance rather than on the specific implications for inductance-based fault location accuracy [5,6,16,20].

This paper develops, validates, and applies a three-sample apparent inductance estimator for fault location in distribution networks. The estimator incorporates median filtering and diagnostic bounding to suppress false estimates caused by transients and noise. Its performance is evaluated across a range of fault types, fault locations, fault resistance levels, and EN 50160-compliant harmonic distortion [10].

The main contributions of this paper are summarized as follows:

- **Algorithm application to passive and active networks:** The apparent inductance-based fault location algorithm is systematically evaluated in the context of PDNs under not only the fundamental frequency but also EN 50160 standard-compliant harmonic distortions. The algorithm application in ADNs highlights how DER penetration alters the physical meaning of the apparent inductance used for distance-to-fault estimation.
- **Signal processing for robust estimation:** A three-sample apparent inductance estimator incorporating adaptive moving-average filtering, IQR-based outlier rejection, and median-based stable-window aggregation is developed and validated, providing reliable inductance estimation under EN 50160 standard-compliant harmonic distortion without dedicated harmonic compensation.

Preprints.org (www.preprints.org) | NOT PEER-REVIEWED | Posted: 19 May 2026 doi:10.20944/preprints202605.1201.v1

- **Quantitative impact assessment:** The influence of fault proximity to the measurement point, system harmonic distortion, and DER penetration levels on the voltage and current measurements, as well as on fault location accuracy, is quantified across various fault types and fault resistances.
- **Practical design guidance for protection engineers:** The study identifies the operating conditions under which the apparent inductance-based method remains reliable and those under which accuracy degrades significantly, providing quantitative performance boundaries that directly guide the adaptation of fault location schemes to the evolving architecture of active distribution networks with high DER penetration.

2. Method for Apparent Inductance-Based Fault Location in DS

2.1. Method Description

The apparent inductance-based algorithm belongs to the family of differential equation algorithms, which represent an important theme in line relaying. This algorithm estimates the fundamental frequency components of voltage and current to determine the impedance to the fault [27], as shown in Figure 1, where a single-line diagram of a faulted medium-voltage feeder is represented.

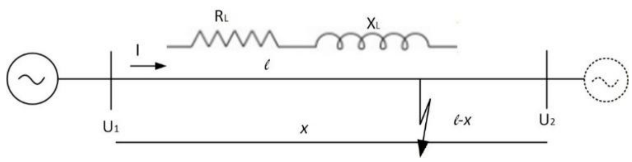

Figure 1. Single-line representation of a medium voltage distribution line.

Differential equation algorithms, by contrast, are based on a system model and can be viewed as parameter estimation problems. Considering the single-phase model case from the faulted line shown in Figure 1, the differential equation relating the voltage and current seen by the relay can be written as shown in (1) [21]

$$u(t) = Ri(t) + L\frac{di(t)}{dt} \tag{1}$$

Since u(t) and i(t) are measured, R and L can be estimated, and the fault distance df can be computed. To avoid numerical differentiation of measured quantities, [27] integrates (1) over two consecutive intervals, yielding (2) and (3).

$$\int_{t_0}^{t_1} u(t)dt = R\int_{t_0}^{t_1} i(t)dt + L[i(t_1) - i(t_0)] \tag{2}$$

$$\int_{t_1}^{t_2} u(t)dt = R\int_{t_1}^{t_2} i(t)dt + L[i(t_2) - i(t_1)] \tag{3}$$

Approximating the integrals with the trapezoidal rule (4) and assuming a uniform sampling interval Δt, equations (2) and (3) become (5) in terms of samples at k, k+1, and k+2.

$$\int_{t_0}^{t_1} u(t)dt = \frac{dt}{2}[u(t_1) + u(t_0)] = \frac{dt}{2}[u_1 + u_2] \tag{4}$$

$$\begin{bmatrix} \frac{\Delta t}{2}(i_{k+1} + i_k) & (i_{k+1} - i_k) \\ \frac{\Delta t}{2}(i_{k+2} + i_{k+1}) & (i_{k+2} - i_{k+1}) \end{bmatrix} \begin{bmatrix} R \\ L \end{bmatrix} = \begin{bmatrix} \frac{\Delta t}{2}(u_{k+1} + u_k) \\ \frac{\Delta t}{2}(u_{k+2} + u_{k+1}) \end{bmatrix} \tag{5}$$

The three voltage and current samples are sufficient to estimate the line resistance R and inductance L [26], as shown in (6) and (7).

$$R = \left[\frac{(u_{k+1}+u_k)(i_{k+2}-i_{k+1})-(u_{k+2}+u_{k+1})(i_{k+1}-i_k)}{(i_{k+1}+i_k)(i_{k+2}-i_{k+1})-(i_{k+2}+i_{k+1})(i_{k+1}-i_k)}\right] \tag{6}$$

$$L = \frac{\Delta t}{2}\left[\frac{(i_{k+1}+i_k)(u_{k+2}+u_{k+1})-(i_{k+2}+i_{k+1})(u_{k+1}-u_k)}{(i_{k+1}+i_k)(i_{k+2}-i_{k+1})-(i_{k+2}+i_{k+1})(i_{k+1}-i_k)}\right] \tag{7}$$

 doi:10.20944/preprints202605.1201.v1

2.2. The Proposed Apparent Inductance Algorithm

The proposed fault-location algorithm estimates the distance to the fault by evaluating the apparent inductance of the distribution feeder section between the measuring point and the fault. The method operates entirely in the time domain and relies on three successive samples of local voltage and current measurements, enabling fast response without the need for phasor estimation or sequence decomposition. Let $u_a(t)$ denote the pre-fault phase-A voltage measured at the feeder head, and $u_{af}(t)$, the corresponding post-fault voltage following fault inception. The instantaneous voltage drop along the faulted feeder section is defined as in (8)

$$u_{drop}(t) = u_a(t) - u_{af}(t) \tag{8}$$

which represents the apparent voltage consumed by the feeder impedance up to the fault location. This quantity inherently captures both resistive and inductive effects of the line segment under fault conditions.

A model-based voltage drop is also computed using the lumped *RL* feeder model as in (9)

$$u_{RL} = R_{line} i_a(t) + L_{line} \frac{di_a(t)}{dt} \tag{9}$$

where $i_a(t)$ is the instantaneous phase-A current, and R_{line} and L_{line} denote the resistance and inductance of the feeder section between the relay location and the fault. The voltage u_{drop} or u_{RL} serves as a model-based reference that allows diagnostic comparison and validation of the estimator behavior. Both are evaluated to assess robustness against measurement noise, DC offsets, and modelling uncertainties.

The apparent inductance is computed from three consecutive samples (k, k+1, k+2) using the closed-form algebraic estimator in (7), which requires no numerical differentiation or frequency-domain processing and is inherently immune to the exponentially decaying DC offset present after fault inception.

2.3. Remarks on Applicability, Assumptions, and Limitations

The proposed method is particularly well-suited to distribution networks, where short line lengths, high *R*/*X* ratios, and non-transposed conductors limit the effectiveness of conventional phasor-based or impedance-relay approaches. By operating directly in the time domain and relying solely on local measurements, the algorithm enables fast and reliable fault location using measurements that are readily available in modern digital relays and power quality recorders.

Nevertheless, the method assumes a predominantly series *RL* representation [23] of the faulted feeder section and neglects shunt capacitance, which is acceptable for short- and medium-length distribution feeders. The accuracy of the distance estimate depends on the correctness of the feeder inductance parameter and may be affected by severe waveform distortion, high harmonic content, or significant infeed from downstream sources.

3. Distribution System Case Study and Modeling

3.1. Distribution Line Model

The system shown in Figure 1 is implemented as a 22 kV, 50 Hz, 20 km distribution line with AlFe ACSR DOG conductors. Its model was implemented, simulated, and tested using MATLAB codes and MATLAB/Simulink version R2023b, as shown in Figure 2. Various types of faults were considered to occur in the system at 0.04 seconds, including single-line-to-ground, line-to-line, double-line-to-ground, three-phase, and three-phase-to-ground faults. The faults were tested at actual fault locations of 3 km, 7 km, 12 km, and 18 km. The impact of fault resistance, as well as the presence of 3rd, 5th, 7th, and 9th harmonics, was also evaluated.

Preprints.org (www.preprints.org) | NOT PEER-REVIEWED | Posted: 19 May 2026 doi:10.20944/preprints202605.1201.v1

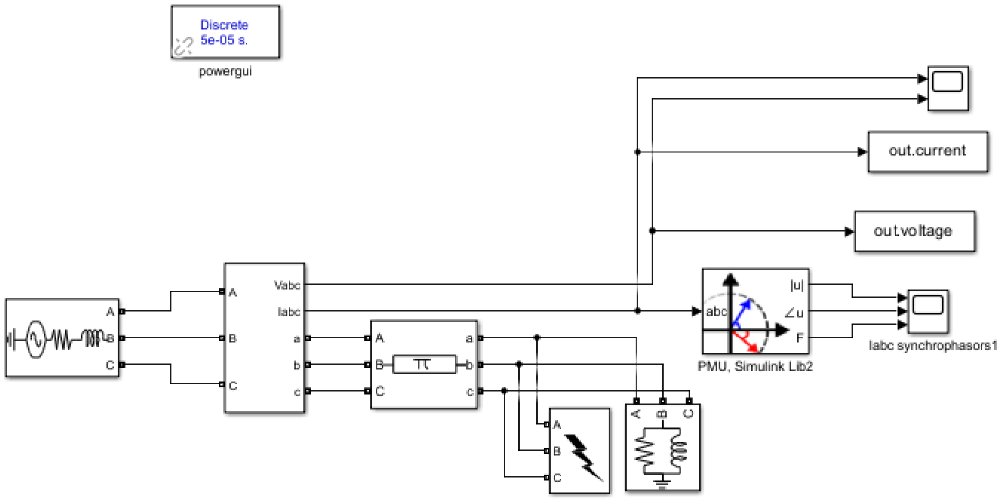

Figure 2. Faulted distribution line model.

The source is a 22 kV, 50 Hz three-phase voltage source feeding a load of 8 MW active and 2.6295 Mvar reactive power. Typical line parameters for the ACSR DOG conductors are given in Table 1.

Table 1. Typical parameters of an ACSR DOG (AlFe) 22 kV overhead distribution line.

Parameter	Positive Sequence (1)	Zero Sequence (0)
Resistance, R (Ω/km)	0.30 - 0.32	0.7 - 1.2
Inductance, L (mH/km)	1.1 - 1.3	3.5 - 4.5
Reactance, X at 50Hz (Ω/km)	0.35 - 0.41	1.1 - 1.4
Capacitance (μF/km)	0.008 - 0.012	0.003 - 0.005

3.2. Specific Operating Aspects Tested

This section examines the operating conditions that affect the accuracy of the apparent inductance-based estimator. These inclTableude the vicinity and remoteness of the fault with respect to the measuring relay, the impact of the fault resistance levels as well as the presence of harmonics. To be more realistic, various effects faced in real-life distribution systems, such as measurement noise and instrument transformer inaccuracies, have been considered.

The distance between the measuring device and the fault is a key factor in the analysis. If the fault occurs closer to the measuring point, the faulted loop is too small with low impedance. This results in the sudden voltage collapse to nearly zero, causing the fault current to rise to very high values. On the other hand, the fault occurring at the remote end with respect to the measuring unit position is accompanied by a slight decrease in voltage and an increase in current, as depicted in Figure 6.

Fault resistance also significantly affects protection systems, and fault locators in particular. The impact may differ depending on the system's earthing method: solidly earthed, resistance earthed, compensated, or unearthed network. In any case, when a fault occurs with a certain fault resistance, this resistance is in series with the impedance of the faulted portion of the line and increases the impedance. In this case, inductance, which is the basis of the presented algorithm, is practically not affected, but still, the impact of the fault resistance on the estimator accuracy is assessed.

The third aspect evaluated is harmonic distortion. The 3rd, 5th, 7th, and 9th harmonics, which are the most commonly found in distribution networks, have been considered. Equations (10) and (11) describe the impact of the harmonic of order h in the system, which amplifies the signal by $h\omega$ after differentiation.

$$u_h(t) = Ri_h(t) + L\frac{di_h(t)}{dt} \quad (10)$$

$$\frac{di_h}{dt} = \sum_h h\omega I_h \cos(h\omega t) \quad (11)$$

 doi:10.20944/preprints202605.1201.v1

The harmonic level limits provided by the standard EN 50160 related to voltage disturbances and voltage characteristics in public distribution systems have been considered, and the robustness of the proposed algorithm estimator has been evaluated. These limits are expressed as percentages of the nominal voltage at the supply terminals and are 5%, 6%, 5%, and 1.5% for the 3rd, 5th, 7th, and 9th harmonics, respectively [10].

3.3. Proposed Methodology Overview in ADNs

The apparent inductance-based algorithm is here extended and evaluated for ADNs with varying DER penetration levels, following four stages: (i) system modeling under active network conditions, (ii) signal acquisition and conditioning, (iii) apparent inductance and fault location estimation, and (iv) performance assessment.

Unlike conventional passive feeders, ADNs are characterized by multi-source fault current contributions and bidirectional power flows, which alter the voltage and current waveforms measured at the substation. The method is applied to a 22-kV distribution feeder equipped with converter-based DERs connected downstream of the measurement point, as illustrated in Figure 3. Various case scenarios have been tested involving different fault types, fault resistances, and a range of DER penetration levels. For each case, the algorithm estimates the fault distance using locally measured voltages and currents, thus preserving the single-ended nature of the method. This enables a direct assessment of how network activeness affects the apparent inductance concept.

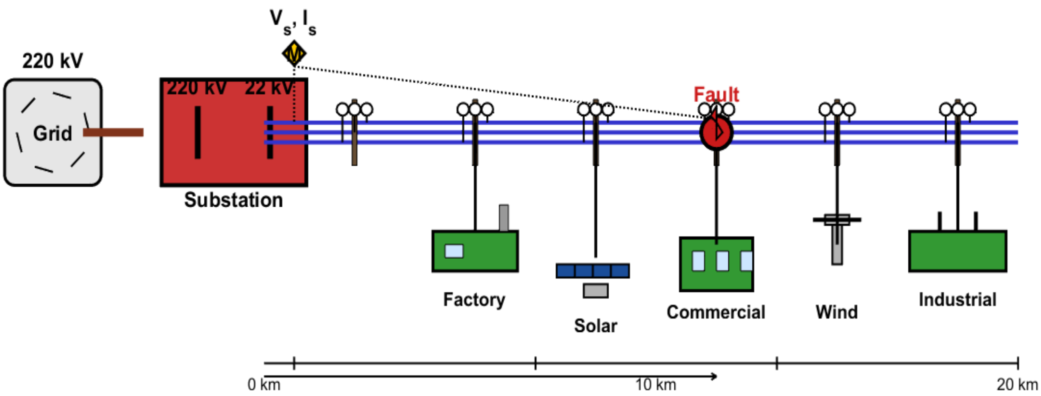

Figure 3. 22kV active distribution network, physical layout.

The system comprises a utility grid connection (left), a 220/22 kV substation, and a 20 km distribution line with distribution poles. Three loads (Factory, commercial, and industrial) and two DER installations (solar and wind) are connected along the line. Different types of faults are simulated at 10 km from the substation. Voltage and current measurements are taken at the grid side. The line conductors are ACSR (AlFe), with the same parameters as in Table 1.

3.4. Modeling of the Active Distribution Network

The feeder is modeled as a series combination of resistance and inductance, with parameters derived from ACSR DOG (AlFe) conductor data. The upstream grid is represented by a Thevenin equivalent consisting of a voltage source and internal impedance (*Rs, Ls*). The fault is modeled as a shunt branch with resistance R_f located at a known distance da from the substation.

DERs are modeled as controlled current sources connected at the downstream end of the feeder. Their contribution during faults is scaled according to the penetration level, defined as the ratio between DER-rated power and feeder load demand. The considered penetration levels of 0%, 20%, 50%, and 80% reflect typical operating conditions of active distribution systems in different case scenarios.

 doi:10.20944/preprints202605.1201.v1

During faults, DER fault current contribution is assumed to be limited and controlled, consistent with the behavior of inverter-based resources [29,30]. This reflects a key ADN characteristic: fault currents no longer scale linearly with impedance, directly affecting inductance-based estimation.

3.5. Signal Acquisition and Conditioning

Voltage and current at the substation are sampled at a fixed frequency of 10 kHz. Measurement noise and instrument transformer ratio errors are added to emulate realistic protection system conditions. A signal-to-noise ratio (SNR) of 65 dB for the voltage and 63 dB for the current has been considered. The maximum error of 0.2% of the actual CT current and 0.1% of the actual PT voltage has been considered. However, for change-based measurements, systematic constant errors do not affect the process outcome. The measured signals are processed through a short moving-average filter to mitigate high-frequency noise while preserving the fundamental transient dynamics required for time-domain estimation. This adaptive filtering ensures smooth apparent inductance convergence and stable numerical derivatives.

3.6. Apparent Inductance Estimation Modeling in Active Distribution Networks

The feeder section between the measurement point and the fault is modeled as a series R–L circuit [25]. Neglecting capacitance effects (which is acceptable for short- and medium-length distribution feeders) during the short post-fault window, the governing equation is given in equation (1). The equivalent circuit of the medium voltage distribution line in question is depicted in Figure 4.

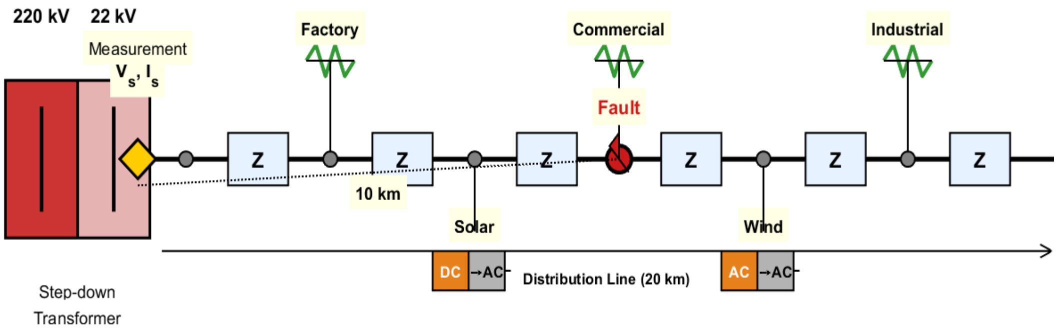

Figure 4. Equivalent circuit, 22 kV distribution network.

Using three consecutive samples of voltage and current, the apparent inductance is estimated through a discrete-time formulation derived from the trapezoidal integration rule [26,27] following the formulation in (6) and (7).

This formulation is equally applied in the ADN case to isolate performance variations attributable to DER penetration.

3.7. Fault Location Estimation

To enhance robustness, the apparent inductance is computed over a post-fault time window after transient settling. Outliers are removed using an interquartile range (IQR) criterion [28], and the median value of the remaining samples is selected as the representative inductance estimate, Lapp. The estimated fault distance df is obtained as in (12)

$$d_f = \frac{L_{app}}{L_{per\ km}} \tag{12}$$

where L_{app} denotes the line apparent inductance and $L_{per\ km}$, the inductance per unit length of the feeder.

3.8. Performance Assessment Strategy

The proposed methodology is validated through a comprehensive set of simulation scenarios reflecting realistic DS operating conditions. Performance is evaluated using the following metrics: Estimated distance to fault location, d_f, and actual fault location D_a. Absolute error and relative error are respectively given in (13) and (14)

$$X_e = \left|d_f - D_a\right| \tag{13}$$

$$P_e = \left|\frac{d_f - D_a}{D_a}\right| \text{x } 100 \tag{14}$$

The assessment covers fault type, fault resistance (low- and high-impedance), fault location, EN 50160-compliant harmonics, and DER penetration levels. The overall approach is summarised in Figure 5.

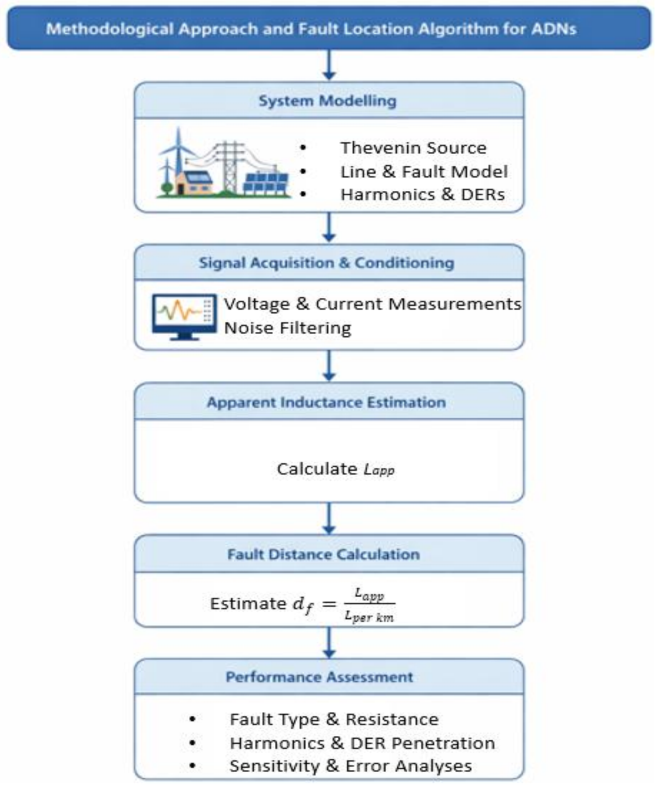

Figure 5. Methodological approach and apparent inductance algorithm.

4. Simulation Results and Discussions

4.1. Fault Simulation in Different Working Conditions

Figure 6 illustrates the voltage and current waveforms recorded at the measurement point for two representative fault scenarios that bound the range of conditions studied in this work. Figure 6(a) shows a three-phase fault at the remote end of the feeder: the voltage sag is moderate, and the fault current surge is relatively small, reflecting the significant line impedance between the measurement point and the fault. The apparent inductance estimated from these measurements is therefore high, correctly indicating a fault far from the substation. Figure 6(b) shows a double-line-to-ground fault near the measurement point: the voltage collapses sharply, and the fault current surge is large, as little line impedance separates the relay from the fault. The apparent inductance is correspondingly low, indicating a close fault. Voltage and current waveforms illustrating fault proximity effects are shown in Figure 6: (a) a three-phase fault at the remote end and a double-line-to-ground fault near the relay (b).

Preprints.org (www.preprints.org) | NOT PEER-REVIEWED | Posted: 19 May 2026 doi:10.20944/preprints202605.1201.v1

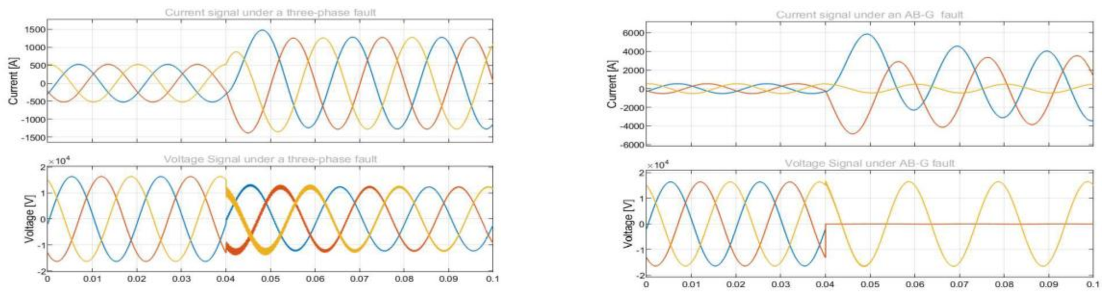

a b

Figure 6. Voltage and current waveforms: (a) three-phase fault far from the measuring unit, (b) double-line-to-ground fault near the measurement point.

These two cases illustrate the fundamental operating principle of the apparent inductance algorithm: the closer the fault, the smaller the estimated inductance, and the more severe the voltage collapse and current surge observed at the relay. This proximity-to-inductance relationship holds under ideal sinusoidal conditions and forms the basis for the systematic performance evaluation conducted in Sections 4.2 through 4.4, where the effects of fault resistance, harmonic distortion, and DER penetration on this relationship are progressively introduced and quantified.

4.2. Fault Location with the 3-Sample Apparent Inductance Algorithm at Fundamental Frequency

A representative case in Figure 7 shows the algorithm applied to a single-phase fault at 12 km with R_f of 5 Ω under sinusoidal conditions. The estimated inductance of 14.174 mH corresponds to a fault location of 11.811 km, with a relative error of 1.57%.

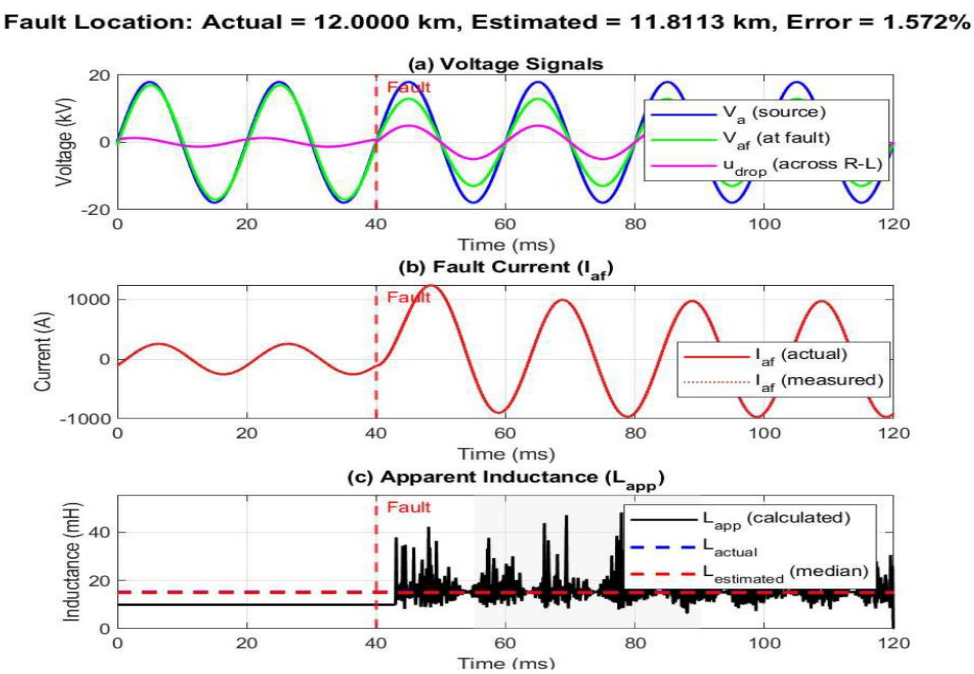

Figure 7. Apparent inductance algorithm fault location under PDN, 50 Hz.

For a comprehensive analysis of the system that considers three fault types (A-G, AB, ABC-G), three actual fault distances (2 km, 10 km, and 19 km), and two different fault resistances (low R_f of 5 Ω and high R_f of 500 Ω) under ideal sinusoidal conditions, the proposed apparent-inductance-based fault-location method demonstrates consistently high accuracy across all tested fault types, resistances, and locations. For low-resistance faults, the relative error remains very small for all scenarios, confirming the strong convergence properties of the inductance estimator and its weak

Preprints.org (www.preprints.org) | NOT PEER-REVIEWED | Posted: 19 May 2026 doi:10.20944/preprints202605.1201.v1

sensitivity to operating point variations. Even for high-resistance faults, where the fault current magnitude is significantly reduced, the enhanced algorithm, combining adaptive filtering, delayed stable-window selection, and *R–L* compensation, maintains reliable performance, with errors remaining within acceptable limits. The comprehensive analysis results are summarized in Table 2 and compared in Figure 8.

Table 2. Comprehensive analysis of the system under fundamental frequency.

Fault	R_f (Ω)	Da (km)	d_f (km)	Xe (km)	Pe (%)
AG	5	2	1.9711	0.0289	1.445
AG	500	2	1.8911	0.1089	5.447
AG	5	10	9.8585	0.1415	1.415
AG	500	10	9.0223	0.9777	9.777
AG	5	19	18.6628	0.3372	1.775
AG	500	19	18.1739	0.8261	4.348
AB	5	2	1.9868	0.0132	0.661
AB	500	2	2.0013	0.0013	0.063
AB	5	10	9.8949	0.1051	1.051
AB	500	10	9.3999	0.6001	6.001
AB	5	19	18.7140	0.2860	1.505
AB	500	19	17.4278	1.5722	8.274
ABCG	5	2	1.9888	0.0112	0.560
ABCG	500	2	1.8130	0.1870	9.349
ABCG	5	10	9.8443	0.1557	1.557
ABCG	500	10	9.9113	0.0887	0.887
ABCG	5	19	18.9121	0.0879	0.463
ABCG	500	19	18.1475	0.8525	4.487

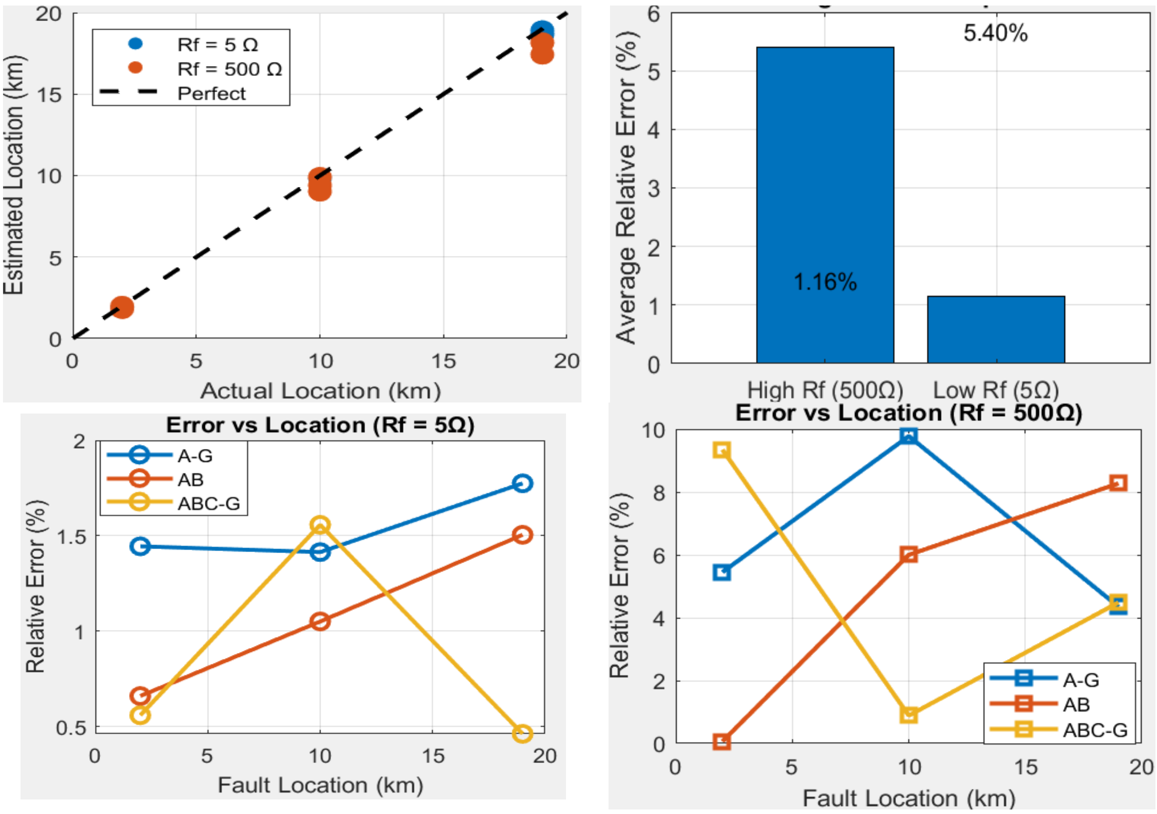

Figure 8. Comprehensive analysis result comparison under 50 Hz.

 doi:10.20944/preprints202605.1201.v1

4.3. Fault Location with the 3-Sample Apparent Inductance Algorithm Under Harmonics

The algorithm was applied to the system under EN 50160-compliant 3rd, 5th, 7th, and 9th harmonics [10]. Figure 9 illustrates a representative case: single-phase fault at 12 km, R_f of 5 Ω, yielding an estimated location of 11.725 km (relative error 2.29%), only marginally higher than the 50 Hz baseline (1.57%).

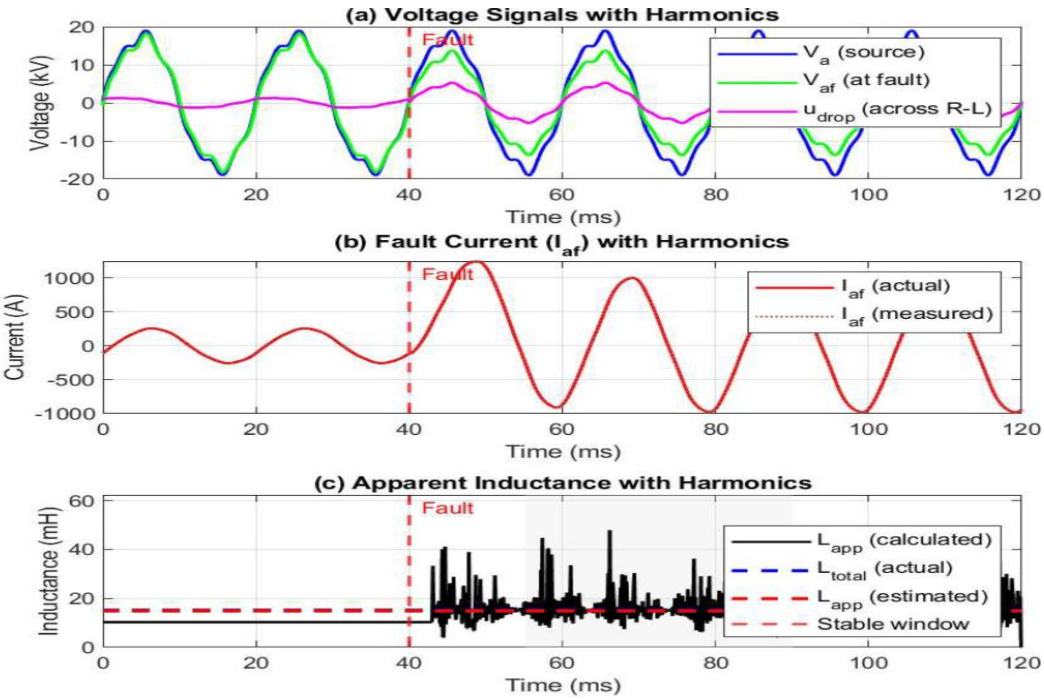

Figure 9. Apparent inductance algorithm fault location under harmonics.

The comparison of the voltage harmonic spectrum before and after fault inception shows that the harmonic content remains essentially bounded within the EN 50160 limits, even under fault conditions. While the fault introduces a noticeable increase in the fundamental and low-order harmonic magnitudes due to the abrupt change in network impedance, no abnormal harmonic amplification is observed. This confirms that the fault primarily affects the signal amplitude rather than its spectral composition, validating the use of harmonic-robust signal processing and supporting the reliability of the proposed fault-location algorithm in harmonically distorted but standards-compliant environments. This is depicted in Figure 10.

doi:10.20944/preprints202605.1201.v1

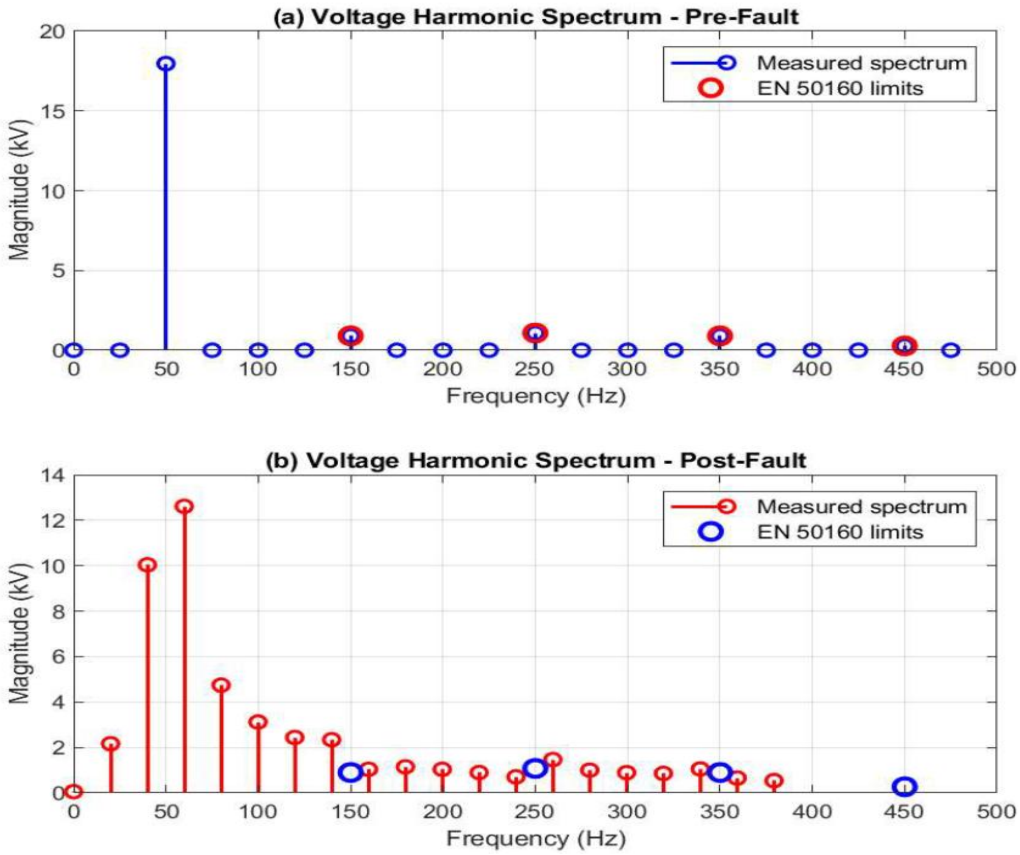

Figure 10. Voltage harmonic spectrum comparison.

The comprehensive analysis conducted for the system with EN 50160–compliant 3rd, 5th, 7th, and 9th harmonics is presented in this subsection, and the results are summarized in Table 3. The analysis demonstrates that the proposed fault-location algorithm remains robust across different fault types, fault resistances, and fault locations. While the presence of harmonics slightly increases the variability of voltage and current measurements, the resulting impact on location accuracy is limited, particularly for low-resistance faults where errors remain consistently small.

Table 3. Comprehensive analysis of the system under EN 50160 standard-compliant harmonics.

Fault	R_f (Ω)	Da (km)	d_f (km)	Xe (km)	Pe (%)
AG	5	2	1.9716	0.0284	1.418
AG	500	2	1.6543	0.3457	17.283
AG	5	10	9.7986	0.2014	2.014
AG	500	10	9.2395	0.7605	7.605
AG	5	19	18.5393	0.4607	2.425
AG	500	19	19.5264	0.5264	2.771
AB	5	2	1.9777	0.0223	1.113
AB	500	2	1.970	0.0030	0.149
AB	5	10	9.8682	0.1318	1.318
AB	500	10	9.3457	0.6543	6.543
AB	5	19	18.7627	0.2373	1.249
AB	500	19	17.0524	1.9476	10.250
ABCG	5	2	1.9792	0.0208	1.041
ABCG	500	2	1.8302	0.1698	8.488
ABCG	5	10	9.9036	0.0964	0.964
ABCG	500	10	9.9027	0.0973	0.973
ABCG	5	19	18.7821	0.2179	1.147
ABCG	500	19	17.8648	1.1352	5.975

Preprints.org (www.preprints.org) | NOT PEER-REVIEWED | Posted: 19 May 2026 doi:10.20944/preprints202605.1201.v1

For high-resistance faults, a moderate increase in estimation error is observed, especially for ground-involved faults at short distances; however, the enhanced algorithm incorporating adaptive filtering and resistance–inductance compensation effectively mitigates this degradation. Overall, the results confirm that realistic harmonic distortion does not compromise the reliability of the method, validating its suitability for practical deployment in modern distribution networks operating under non-ideal power-quality conditions. The analysis results are compared in Figure 11.

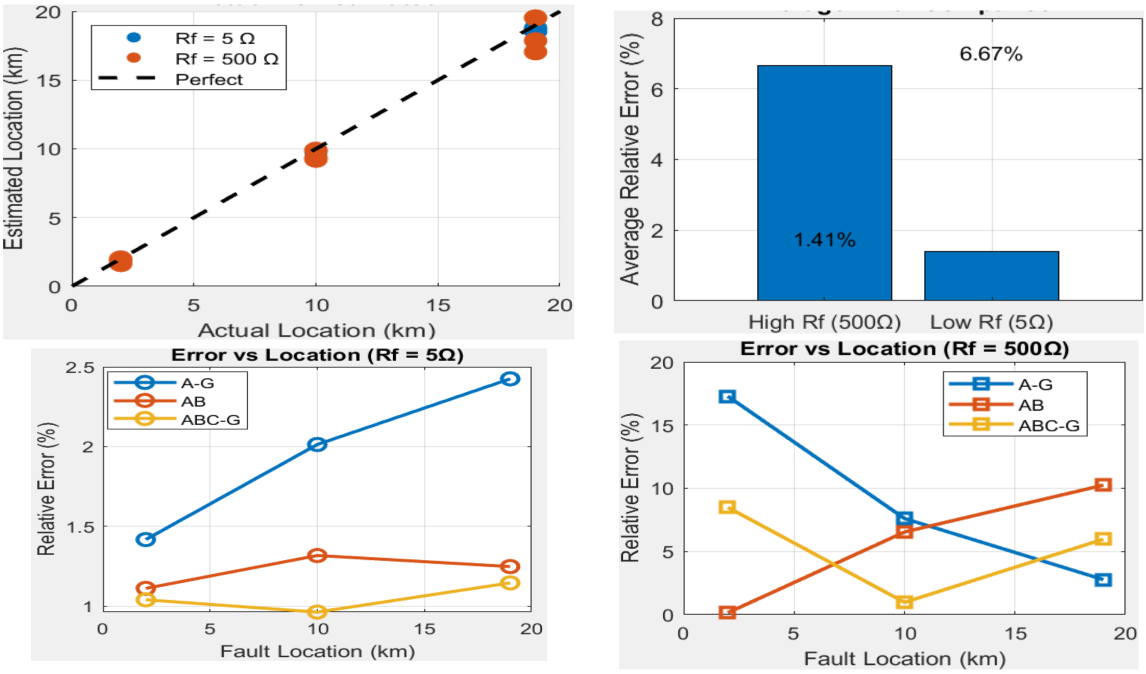

Figure 11. EN 50160 standard-compliant comprehensive analysis result comparison.

4.4. Comparison Between the Comprehensive Analysis Under Fundamental Frequency and Harmonics

Figure 12 compares relative errors under 50 Hz and EN 50160-compliant harmonic conditions. Most data points cluster near the unity line, confirming accuracy preservation under typical power-quality distortion. High-resistance ground faults show the largest sensitivity; in several scenarios, the harmonic case yields comparable or slightly improved accuracy due to adaptive filtering and median-based aggregation.

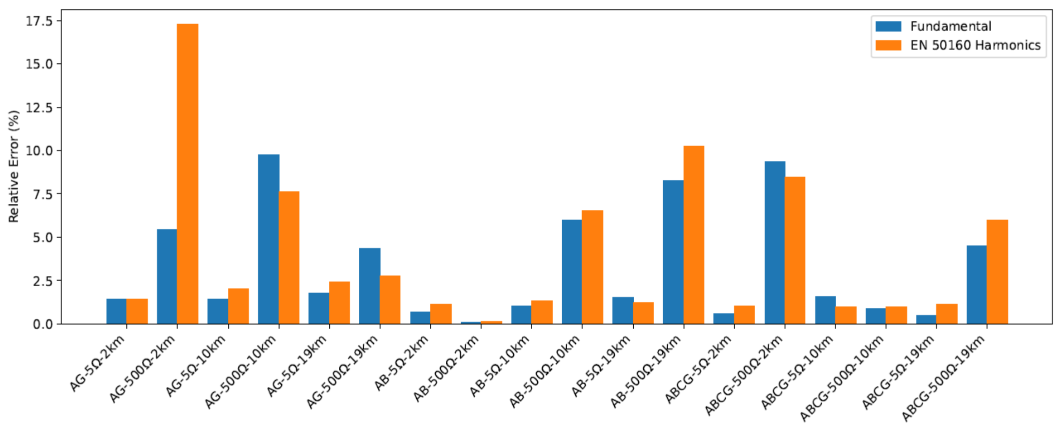

Figure 12. Comparison between the comprehensive analysis for the system under fundamental frequency and that under EN 50160-compliant harmonics.

 doi:10.20944/preprints202605.1201.v1

4.5. Fault Location with the 3-Sample Apparent Inductance Algorithm in ADNs

The proposed fault location algorithm was evaluated in an active distribution network, where the impact of DERs on signal measurements and the fault location accuracy were assessed. Three representative case scenarios consisting of A-G with R_f of 5Ω at 0% and 20% of DER penetration, as well as ABC-G with R_f of 500 ohms at 80% DER, were presented in Figures 13 to 15. A comprehensive set of scenarios was also analyzed for an actual fault location of 10 km. Three fault types (A–G, AB, and ABC–G), two fault resistances (5 Ω, standing for low impedance faults, and 500 Ω representing the high impedance faults) were applied, under different DER penetration levels (0%, 20%, 50%, and 80%). The graphical representation of the single-phase low-impedance fault with 0% DER penetration is shown in Figure 13.

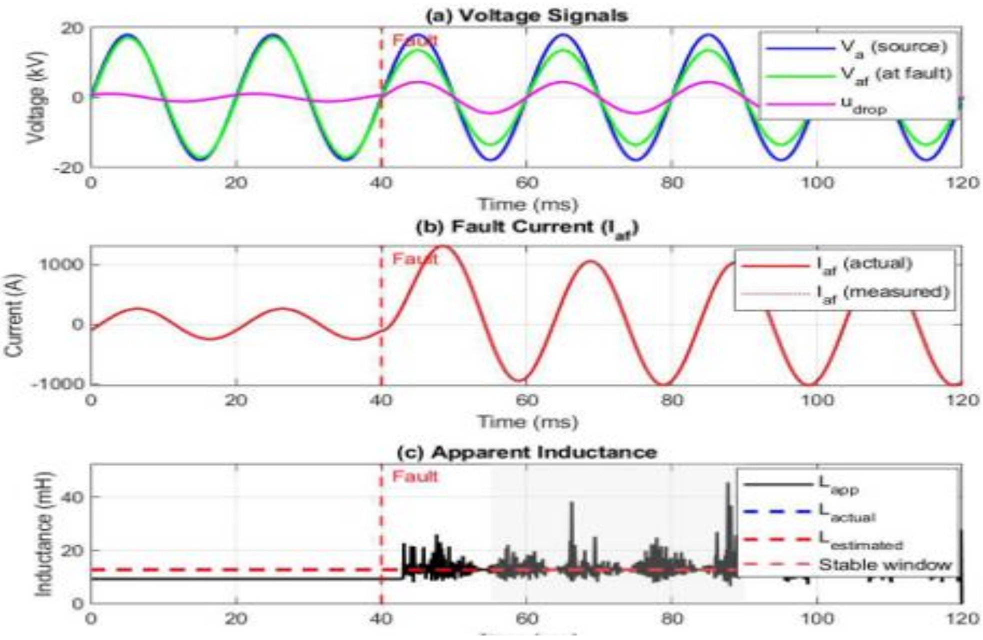

Figure 13. Single-phase fault, R_f of 5 ohms at 10km with 0% DER penetration.

The apparent inductance algorithm for fault location, applied in a distribution network with 0% DER penetration, under a single-phase low-impedance fault (R_f of 5 Ω) located at 10km, demonstrates higher performance, with a relative error of 1.246%. The easiest fault-location case among all scenarios tested at 0% DER penetration was ABC-G, 5 ohms, with a relative error of 0.018%, as shown in Table 4. The results of a single-phase low impedance fault (R_f of 5 Ω) at 20% DER penetration are depicted in Figure 14.

 doi:10.20944/preprints202605.1201.v1

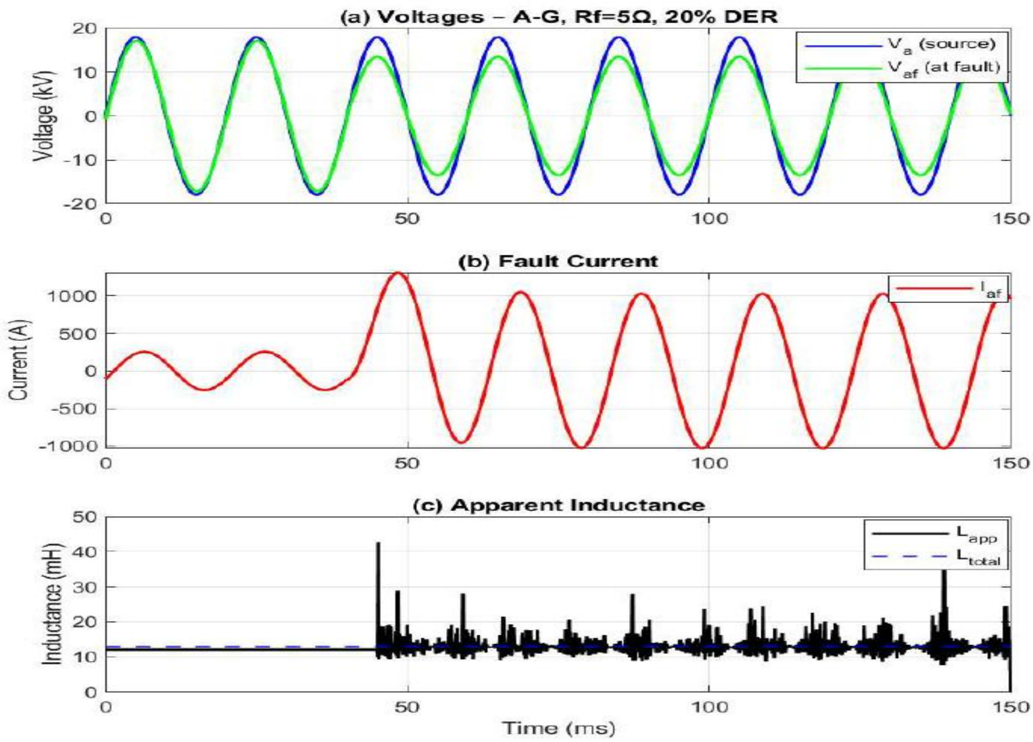

Figure 14. Single-phase fault, R_f of 5 ohms at 10km with 20% DER penetration.

The relative error exhibited by the proposed fault location algorithm for the case of A-G, 5 ohms, 20% DER penetration is 2.246%, which is higher than that of the same fault type at 0% DER penetration (1.246%), and remarkably lower than that of the same fault at 50% and 80% DER penetrations, which are respectively 3.246% and 4.246%. This demonstrates the impact of increasing intermittent DER penetrations on the accuracy of the fault location algorithm in distribution systems.

Another aspect that significantly affects the accuracy of the apparent inductance estimation and, consequently, the fault location determination is the fault resistance. In the context of the present work, two cases in terms of fault resistance have been considered: low-impedance faults and high-impedance faults. The examples of low impedance faults were discussed above (Figure 13 and Figure 14). In Figure 15, an example of a high impedance three-phase fault (R_f of 500 ohms) occurring at 10 km along an ADN with 80% DER penetration is depicted. The low fault current signal due to the high fault resistance, the signal alteration, and the multi-source nature of this fault due to the high penetration of DER imply a relative error of 23.774%, making it one of the hardest to locate. The worst-case was A–G at 500 Ω and 50% DER (Pe of 29.028%), for which, in addition to the low fault current and altered signal caused by the high fault resistance and high DER penetration, the system imbalance and zero-sequence bias further increase the challenges in locating such a high-impedance single-phase fault.

 doi:10.20944/preprints202605.1201.v1

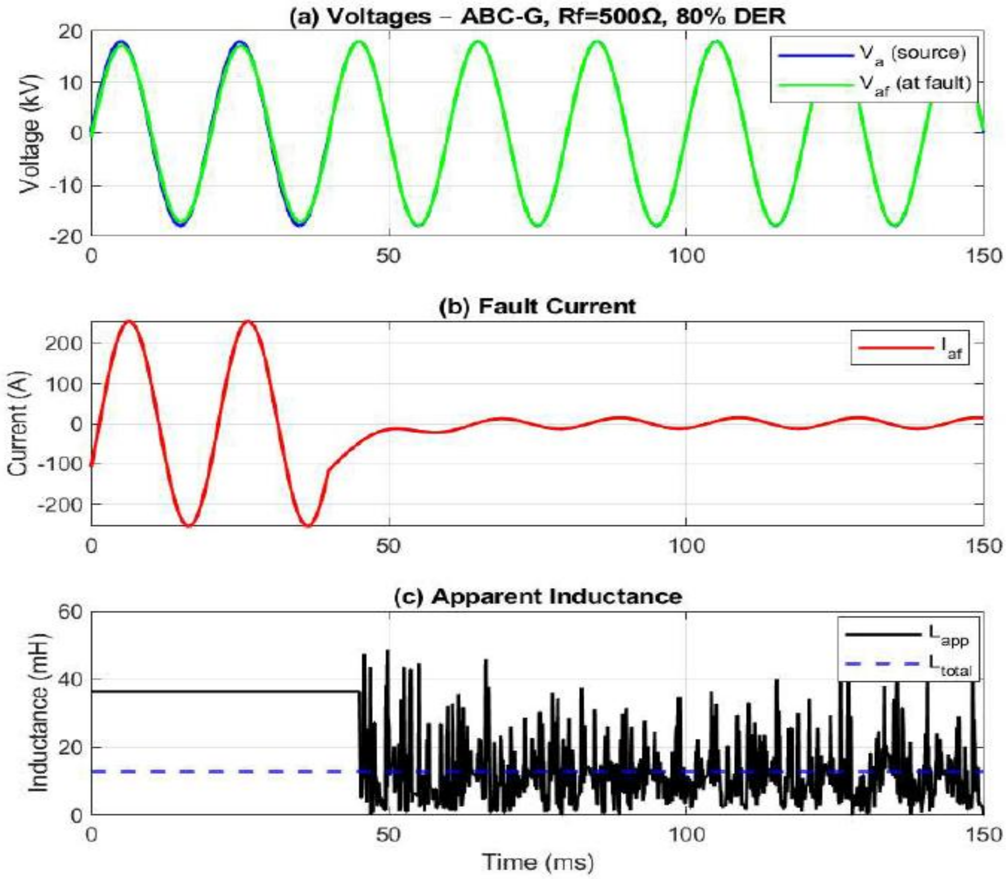

Figure 15. Three-phase fault, R_f of 500 ohms at 10km, with 80% DER penetration.

The full results across all fault types (A–G, AB, ABC–G), two fault resistances (5 Ω and 500 Ω), and DER penetration levels (0–80%) are summarized in Table 4 and compared in a graphical representation in Figure 16, and a bar chart in Figure 17.

In general, the comprehensive analysis results have confirmed that (1) higher impedance faults are harder to locate than their corresponding low impedance faults. (2) ADNs are more challenging for fault locators, and challenges increase tremendously with the increase of DER penetration. (3) Single-phase-to-ground faults are the hardest to locate due to the system imbalances and zero sequence bias, followed by the line-to-line faults for the same reasons, while three-phase faults are the easiest to locate due mainly to their symmetric aspect.

Preprints.org (www.preprints.org) | NOT PEER-REVIEWED | Posted: 19 May 2026 doi:10.20944/preprints202605.1201.v1

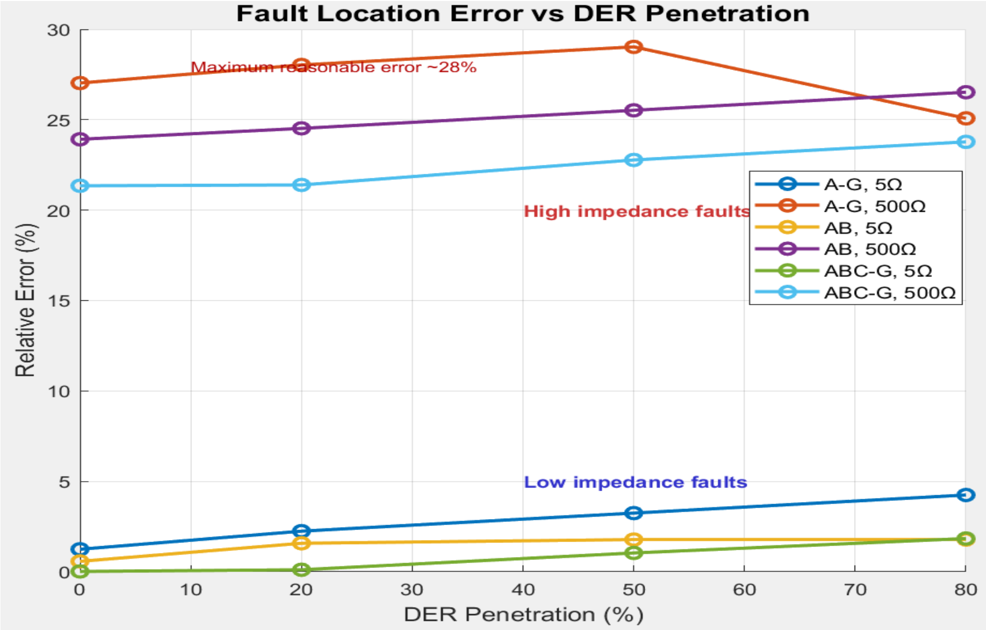

Figure 16. Comparison of different faults with R_f and different DER penetrations.

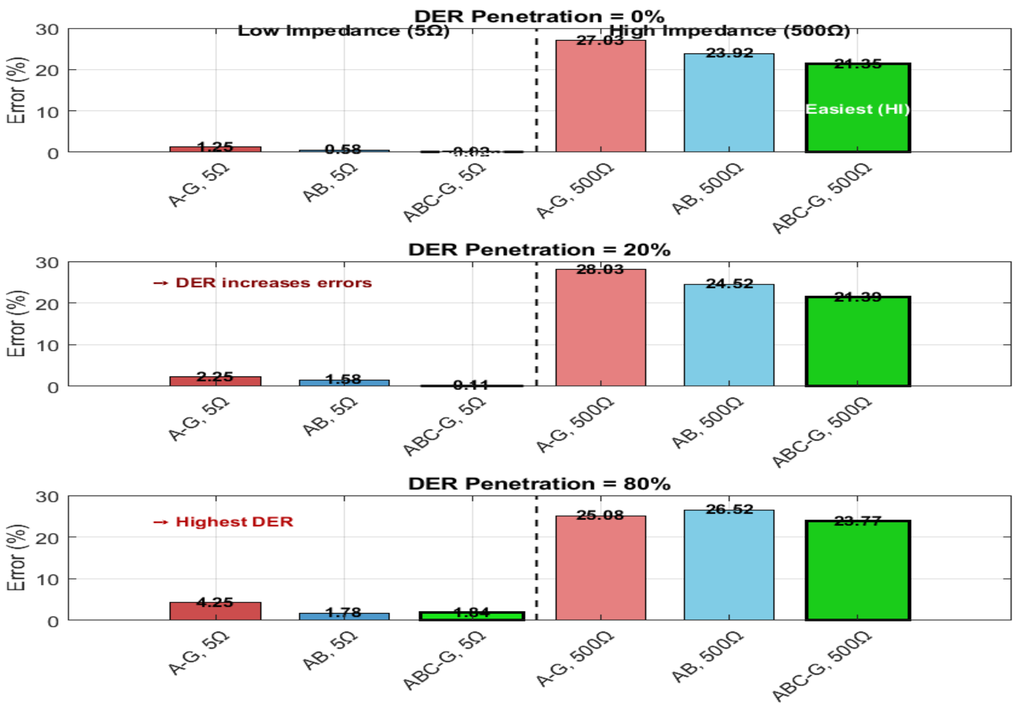

Figure 17. Chart comparison of different faults with R_f and different DER penetrations.

Table 4. Different fault simulation results with different levels of der penetration.

Fault	R_f (Ω)	DER pen [%]	D_a (km)	d_f (km)	Xe (km)	Pe (%)
AG	5	0	10	9.8754	0.1246	1.246
AG	500	0	10	7.2972	2.7028	27.028
AG	5	20	10	9.7754	0.2246	2.246
AG	500	20	10	7.1972	2.8028	28.028
AG	5	50	10	9.6754	0.3246	3.246
AG	500	50	10	7.0972	2.9028	29.028
AG	5	80	10	9.5754	0.4246	4.246
AG	500	80	10	7.4924	2.5076	25.076

Preprints.org (www.preprints.org) | NOT PEER-REVIEWED | Posted: 19 May 2026 doi:10.20944/preprints202605.1201.v1

AB	5	0	10	9.9423	0.0577	0.577
AB	500	0	10	7.6082	2.3918	23.918
AB	5	20	10	9.8423	0.1577	1.577
AB	500	20	10	7.5480	2.4520	24.52
AB	5	50	10	9.8218	0.1782	1.782
AB	500	50	10	7.4480	2.5520	25.52
AB	5	80	10	10.1784	0.1784	1.784
AB	500	80	10	7.3480	2.6520	26.52
ABCG	5	0	10	10.0018	0.0018	0.018
ABCG	500	0	10	7.8652	2.1348	21.348
ABCG	5	20	10	9.9887	0.0113	0.113
ABCG	500	20	10	7.8608	2.1392	21.392
ABCG	5	50	10	9.8959	0.1041	1.041
ABCG	500	50	10	7.7226	2.2774	22.774
ABCG	5	80	10	9.8160	0.1840	1.84
ABCG	500	80	10	7.6226	2.3774	23.774

4.6. Sensitivity Analysis

A comprehensive sensitivity analysis was conducted to quantify the robustness of the proposed fault-location algorithm under realistic operating conditions. Five parameters were varied one at a time, with all others held at their nominal values: fault resistance R_f (5–1000 Ω), voltage measurement SNR (45–75 dB), pre-fault load current (50–300 A), total harmonic distortion THD (0–18.8 %), and distributed energy resource (DER) penetration (0–80 %). For each parameter, the average relative location error was analyzed for each fault type, as shown in Figs. 17–21.

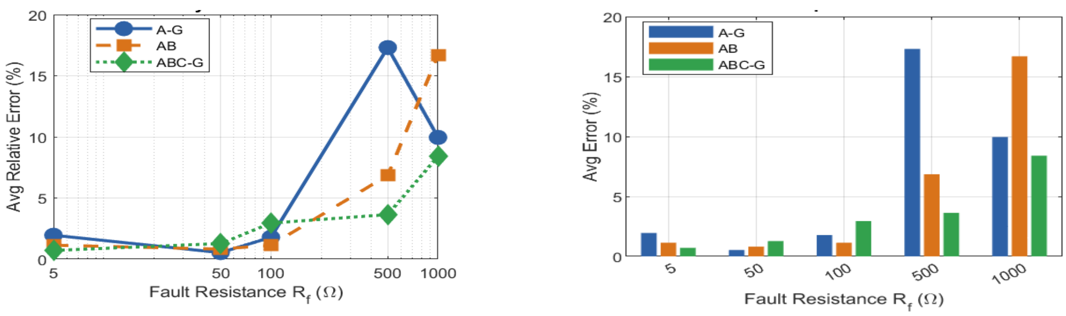

Figure 17. Sensitivity to fault resistance.

Fault resistance is the dominant source of accuracy degradation of the proposed fault location method. At low values (R_f of 5Ω), the algorithm achieves mean errors of 1.95%, 1.14%, and 0.71% for A-G, AB, and ABC-G faults, respectively. Performance deteriorates remarkably beyond R_f of 100 Ω, reaching 17.3 % for A-G and 16.7 % for AB faults at 1000 Ω. The high fault resistance reduces the voltage drop across the line impedance, compressing the observable signal and increasing the uncertainty in the apparent inductance estimate.

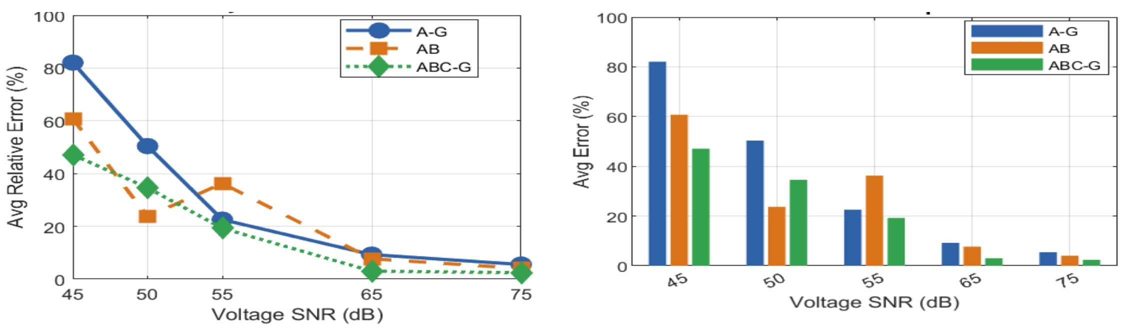

Figure 18. Sensitivity to measurement SNR.

SNR has a strong impact on all fault types. At 45 dB, average errors reach 82%, 61%, and 47% for A-G, AB, and ABC-G, respectively, making the algorithm unreliable. Performance improves rapidly with SNR, falling below 10 % for all fault types at 65 dB (the nominal operating point) and below 5.5 % at 75 dB. These results prove that an accurate inductance-based fault location method requires proper signal conditioning and anti-aliasing filtering. A minimum SNR of around 55 dB is necessary to keep average errors within a practically acceptable range (around 25%). The strong SNR sensitivity confirms that measurement noise is not a "constant systematic error" that cancels in differential calculations, but a random additive white Gaussian noise (AWGN) that directly corrupts the finite-difference approximations of $\frac{di}{dt}$ and $\frac{du}{dt}$, undermining the inductance estimation.

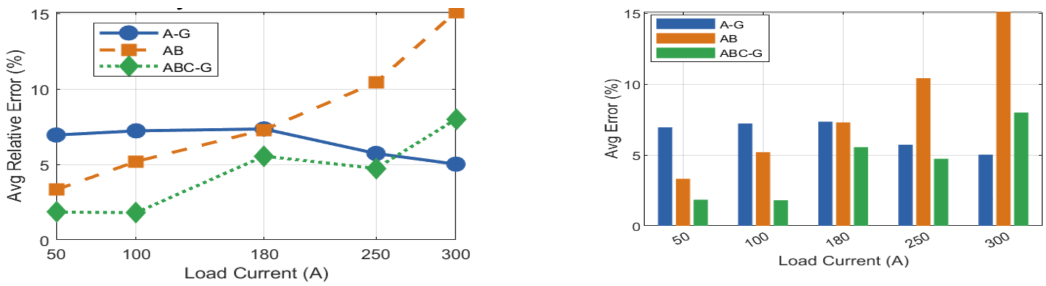

Figure 19. Sensitivity to pre-load current.

Through its repercussions on the signal-to-load-noise ratio, the magnitude of the load current affects algorithm accuracy. At a weak load, for example, at 50 A, respective errors are relatively low: 6.96%, 3.33%, and 1.85% for A-G, AB, and ABC-G faults. As the load increases toward 300 A, the error for AB faults rises to 15.1% and for ABC-G to 8.0%, indicating increased interference from the pre-fault current component within the apparent impedance window. A-G errors remain relatively stable in the range of 5–7.4 %, due to the strong fault-current aspect of single-phase-to-ground events.

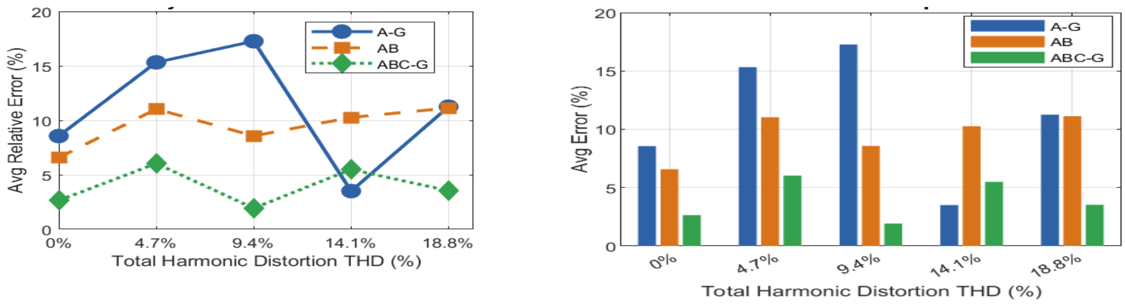

Figure 20. Sensitivity to total harmonic distortion.

Total harmonic distortion (THD), varied from 0 to 18.8 % (double the EN 50160 voltage limits), yields non-monotonic repercussions on the performance of the fault location algorithm. For all fault types, errors vary roughly between 3 and 15%, with no consistent trend, confirming that the moving-average adaptive filter and median-based stable-window estimator jointly eliminate harmonic-induced noise with no systematic bias. The worst-case error at 18.8 % THD remains below 17.3 % (A-G), comparable to the nominal-condition performance (9.4 % THD), proving that the algorithm is adequately robust to the harmonic environment encountered on MV distribution networks.

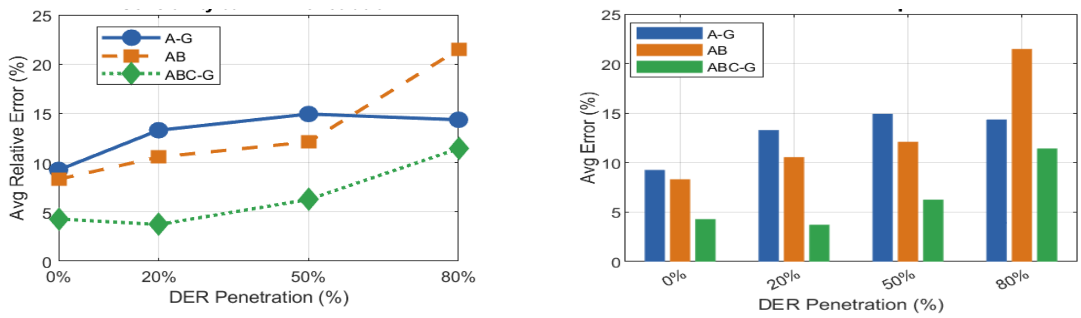

Figure 21. Sensitivity to DER penetration levels.

DER penetration is quantified as the percentage of the nominal load current contributed by inverter-based generation during faults, and ranges from 0 to 80%. DER penetration degrades the algorithm performance through two mechanisms: (a) SNR decay resulting from harmonic and interharmonic content from inverter switching, and (b) augmented transducer ratio errors as a result of bidirectional power flow and nonlinear load aspects. At 0 % DER, errors are 9.3 %, 7.7 %, and 3.0 % for A-G, AB, and ABC-G faults at R_f of 500 Ω. At 80% DER, these increase to approximately 12–18%, reflecting a 30–100% relative increase in error. The impact is more pronounced for high-impedance faults, where the reduced fault-current magnitude makes the algorithm more sensitive to measurement disturbances. However, errors remain below 20% for all fault types across the DER range tested, demonstrating that the algorithm retains practical robustness in ADNs with high penetration of intermittent renewable sources, provided proper filtering and transducer accuracy are well confirmed.

4.7. Performance Comparison with Other Methods

The performance comparison with the most related approaches from the literature is presented in Table 5. It shows that the proposed method achieves comparable accuracy for low-resistance faults in PDNs using only single-ended measurements, with the additional advantages of systematic evaluation under DER penetration and explicit treatment of high-resistance faults.

Table 5. Comparison with related fault location methods.

Method	Ref.	Measurements	System	DER/ADN	Error range
Time-domain Bergeron + spline	[9]	Two-ended D-PMU	MV feeder	No	<1% (low R_f); not evaluated for high R_f
Additional inductance + async. PMU	[12]	Two-ended PMU	MV feeder	No	<1% (low R_f); not evaluated for high R_f
Unsynchronised two-point impedance	[8]	Two substation points	MV overhead	Yes (DG)	<1% (low R_f); high R_f tested, not quantified
Proposed (3-sample apparent inductance)	**This work**	**Single-ended local**	**22 kV, 20 km**	**Yes (0–80%)**	**<2% (low R_f, PDN); <5% (low R_f, ADN); 21–29% (high R_f, ADN)**

4.8. Result Discussion

The algorithm was evaluated through simulation studies covering progressively more realistic operating conditions. In the baseline sinusoidal case in the passive network, the method demonstrated rapid convergence of the apparent inductance after fault inception and consistently low location errors for all tested fault types and locations. These results confirmed the theoretical validity of the inductance–distance relationship and the intrinsic robustness of the time-domain formulation against fault resistance under low-impedance conditions.

When realistic measurement noise and instrument transformer inaccuracies were introduced, a moderate increase in the dispersion of instantaneous inductance estimates was observed. However,

 doi:10.20944/preprints202605.1201.v1

the use of moving-average filtering, physical bounding, and median-based aggregation ensured that the final location estimates remained stable and accurate. This confirms that the proposed approach is well-suited to practical protection environments, where measurement imperfections are unavoidable.

EN 50160-compliant harmonics increased short-term variability of the inductance estimate, particularly immediately after fault inception. Still, steady-state values remained close to the sinusoidal case, and fault-location errors increased only marginally.

The multi-scenario PDN study (A–G, AB, ABC–G; R_f of 5 and 500 Ω; locations at 2, 10, and 19 km) consistently confirmed high accuracy for low-resistance faults. For high-resistance faults, adaptive filtering and *R*–*L* compensation maintained acceptable accuracy. EN 50160-compliant harmonics caused only marginal degradation, and the sensitivity analysis confirmed graceful performance degradation without any abrupt stability loss.

For the apparent inductance–based fault location method in ADNs, different fault types (A–G, AB, and ABC–G), two fault resistances (5 Ω and 500 Ω), and varying DER penetration levels (0–80%) for an actual fault location of 10 km, have been analyzed. For low-impedance faults (R_f of 5 Ω), relative errors remain generally below 5%. The best performance was achieved for the three-phase fault (ABC–G), with an error of almost 0% at 0% DER (0.02%) and remaining low even at high DER penetration (≈1–2%). Single-line-to-ground faults (A–G) were the most challenging, with errors increasing gradually from about 1.25% at 0% DER to 4.25% at 80% DER.

In contrast, high-impedance faults (R_f of 500 Ω) produced significantly higher errors, typically 21–29%. This reflects the reduced fault current and weaker voltage drop, which makes the apparent inductance estimation less stable. The ABC–G faults remained the easiest high-impedance case (~21–24%), while A–G faults showed the poorest performance, occasionally triggering fallback or non-monotonic behavior checks.

Overall, DER penetration consistently increased the fault location error, particularly for high-resistance faults. This is attributed to additional fault current contributions, measurement degradation, and altered network dynamics, which affect the accuracy of inductance-based estimation.

4.9. Study Limitations and Future Work

The present study is subject to different limitations that should be acknowledged. First, both the PDN and ADN test systems are modelled as single radial feeders without branches or laterals. Real distribution networks typically include multiple laterals and branching points, which introduce additional reflected waves and current infeed paths that can affect the apparent inductance estimate. Extending the method to meshed or multi-branch topologies would require addressing fault location ambiguity and adapting the distance-to-fault formula accordingly.

Second, the DER units are represented as ideal controlled current sources with fixed current-limiting behaviour. Practical inverter-based resources exhibit a wider range of control strategies, fault-ride-through profiles, and dynamic responses depending on grid code requirements, which may produce more complex distortions in the fault current waveform than those captured here.

Third, the ADN evaluation is conducted for a single fault distance (10 km from the substation). While this location was chosen to provide a representative mid-feeder scenario, the interaction between DER injection points and fault location may produce different estimation biases at other distances, particularly for faults near the DER connection points.

Finally, the source is modelled as a balanced three-phase Thevenin equivalent, which does not capture the network imbalance inherent to real medium-voltage systems. These limitations define clear directions for future work, including validation on multi-branch feeders, use of detailed inverter models, and a broader range of ADN fault locations.

 doi:10.20944/preprints202605.1201.v1

5. Conclusions

This work developed and evaluated a three-sample apparent inductance-based fault location algorithm for passive and active distribution networks under a comprehensive set of operating conditions, covering three fault types, three fault locations, four fault resistance levels from 5 Ω to 500 Ω, EN 50160 standard-compliant harmonic distortion, and four DER penetration levels from 0% to 80%.

In PDNs under clean sinusoidal conditions, the algorithm achieves relative errors below 2% for low-resistance faults across all fault types and locations, confirming that the inductive component of the line impedance remains strongly correlated with fault distance under ideal conditions. For high-resistance faults at R_f of 500 Ω, errors increase to the range of 5–10%, remaining within practically acceptable limits. Fault type has a marginal influence on accuracy, confirming that line parameters primarily govern estimation quality. EN 50160 standard-compliant harmonic distortion slightly increases estimation variance but introduces no systematic bias or inductance collapse, confirming robustness to realistic harmonic levels without requiring dedicated harmonic mitigation. As shown in Figure 12, most scenarios show comparable accuracy under harmonic and sinusoidal conditions, with high-resistance ground faults showing the largest sensitivity, while the adaptive filtering and median-based aggregation occasionally yield comparable or marginally improved estimates under harmonic excitation.

In ADNs, the algorithm retains high accuracy for low-resistance faults across all fault types and DER penetration levels, with errors below 5% for $R_f \leq 50$ Ω. For high-resistance faults at R_f of 500 Ω combined with high DER penetration at 80%, errors increase to the range of 21–29% depending on the fault type, reflecting the systematic bias introduced by inverter current-limiting behaviour on the apparent inductance estimate. Despite this degradation, the algorithm exhibits graceful performance decay rather than abrupt failure, with monotonically increasing errors across the tested parameter space.

These quantified performance boundaries directly define the operating conditions under which the apparent inductance-based approach remains a reliable single-ended fault location solution, and those under which multi-PMU or DER-aware compensation strategies become necessary. The results provide practical guidance for protection engineers adapting fault location schemes to the evolving architecture of active distribution networks with high DER penetration.

Author Contributions: Conceptualization, O.M. and M.L.; methodology, O.M. and P.T; software, O.M.; validation, O.M., P.T., and M.L.; formal analysis, O.M., A.A., and H.L.; investigation, O.M. and S.T.; resources, O.M. and S.T.; data curation, O.M., A.A.; writing—original draft preparation, O.M.; writing—review and editing, O.M., M.L., P.T., A.A. H.L., and S.T.; visualization, O.M., A.A., S.T., and H.L.; supervision, P.T.; project administration, P.T.; funding acquisition, P.T. All authors have read and agreed to the published version of the manuscript.

Data Availability Statement: The original contributions from the study are included in the article; for further inquiries, please contact the corresponding author.

Funding: This research was funded by the Ministry of Education, Youth and Sports of the Czech Republic, grant number CZ.02.01.01/00/22_008/0004617.

Acknowledgments: This research work has been carried out in the Centre for Research and Utilization of Renewable Energy (CVVOZE). Authors gratefully acknowledge financial support from the Ministry of Education, Youth and Sports of the Czech Republic under project "The Energy Conversion and Storage", No. CZ.02.01.01/00/22_008/0004617 by Programme Johannes Amos Comenius, call Excellent Research. During the preparation of this manuscript/study, the author(s) used Claude AI for the purposes of improving and correcting the MATLAB coding scripts and polishing the final version of the paper. The authors have reviewed and edited the output and take full responsibility for the content of this publication."

 doi:10.20944/preprints202605.1201.v1

Conflicts of Interest: The authors declare no conflicts of interest. The funders had no role in the design of the study; in the collection, analyses, or interpretation of data; in the writing of the manuscript; or in the decision to publish the results.

Abbreviations

The following abbreviations are used in this manuscript:

AND	Active Distribution Network
PDN	Passive Distribution Network
DER	Distributed Energy Resource
FLA	Fault Location Algorithm
PMU	Phasor Measurement Unit
IQR	Interquartile Range
THD	Total Harmonic Distortion
MV	Medium Voltage
R/X	Resistance-to-Reactance ratio
EN 50160	European Standard for Voltage Characteristics in Public Distribution Systems
IEEE	Institute of Electrical and Electronics Engineers
CT	Current Transformer
PT	Potential Transformer
A-G	Single-phase-to-ground fault
AB	Double-phase fault
ABC-G	Three-phase-to-ground fault

Symbols

$u(t)$	instantaneous voltage at the measurement point (V)
$i(t)$	instantaneous current at the measurement point (A)
R	line resistance per unit length (Ω/km)
L	apparent inductance estimated at the measurement point (H)
L_{true}	true line inductance corresponding to the fault distance (H)
R_s	source resistance at the substation equivalent (Ω)
L_s	source inductance at the substation equivalent (H)

 doi:10.20944/preprints202605.1201.v1

d_f estimated fault distance (km)

D_a actual fault distance (km)

R_f fault resistance (Ω)

X_e absolute location error (km)

P_e relative (percent) location error (%)

Δt sampling interval (s)

t_0, t_1, t_2 three consecutive sampling instants (s)

u_k, u_{k+1}, u_{k+2} voltage samples at three consecutive instants (V)

i_k, i_{k+1}, i_{k+2} current samples at three consecutive instants (A)

η_{DER} DER penetration fraction, continuous in [0, 1]

I_{DER} fault current contribution from DER inverters (A)

I_{sub} fault current contribution from the substation source (A)

Z_1, Z_2, Z_0 positive-, negative-, and zero-sequence impedances (Ω)

V_F pre-fault voltage at the fault bus (V)

Z_F fault impedance (Ω)

α load imbalance factor

r_1 line resistance per unit length (Ω/km)

x_1 line reactance per unit length (Ω/km)

ω angular frequency (rad/s)

f fundamental frequency (Hz)

References

1. Guo, L.W.; Xue, Y.D.; Xu, B.Y.; Cai, Y.C.; Zhang, S.F. Research on effects of neutral grounding modes on power supply reliability in distribution networks. *Power System Technology* **2015**, *39*, 2340–2345.
2. Mohd Nasir, M.N.; Sabo, A.; Wahab, N.I.A. A review on synchrophasor technology for power system monitoring. In Proceedings of the IEEE Student Conference on Research and Development (SCOReD), Bandar Seri Iskandar, Malaysia, 2019; pp. 58–62. https://doi.org/10.1109/SCORED.2019.8896339.
3. Pham, T.N.; Shah, R.; Dao, M.N.; Sultanova, N.; Islam, S. Low and medium voltage distribution network planning with distributed energy resources: A survey. *Electr. Eng.* **2024**, *107*, 1797–1828. https://doi.org/10.1007/s00202-024-02535-0.
4. Stefanidou-Voziki, P.; Sapountzoglou, N.; Raison, B.; Dominguez-Garcia, J.L. A review of fault location and classification methods in distribution grids. *Electr. Power Syst. Res.* **2022**, *209*, 108031. https://doi.org/10.1016/j.epsr.2022.108031.
5. Quispe, J.C.; Orduña, E. Transmission line protection challenges influenced by inverter-based resources: A review. *Prot. Control Mod. Power Syst.* **2022**, *7*, 28.

6. Hernández-Santafé, J.D.; Sorrentino, E. Problems and solutions concerning the distance protection of transmission lines connected to inverter-based resources. *Energies* **2025**, *18*, 1375. https://doi.org/10.3390/en18061375.
7. Novosel, D.; Hart, D.G.; Udren, E.; Saha, M.M. Fault location using digital relay data. *IEEE Comput. Appl. Power* **1995**, *8*, 35–50. https://doi.org/10.1109/67.392027.
8. Apostolopoulos, C.A.; Arsoniadis, C.G.; Georgilakis, P.S.; Nikolaidis, V.C. Unsynchronized measurements based fault location algorithm for active distribution systems without requiring source impedances. *IEEE Trans. Power Deliv.* **2022**, *37*, 2071–2082. https://doi.org/10.1109/TPWRD.2021.3103870.
9. Sun, G.; Chen, R.; Han, Z.; Liu, H.; Liu, M.; Zhang, K.; Xu, C.; Wang, Y. Accurate fault location method based on time-domain information estimation for medium-voltage distribution network. *Electronics* **2023**, *12*, 4733. https://doi.org/10.3390/electronics12234733.
10. Markiewicz, H.; Klajn, A. *Voltage Disturbances Standard EN 50160: Voltage Characteristics in Public Distribution Systems*; Wrocław University of Technology: Wrocław, Poland, 2004.
11. Li, Z.; Wan, J.; Wang, P.; Weng, H.; Li, Z. A novel fault section locating method based on distance matching degree in distribution network. *Prot. Control Mod. Power Syst.* **2021**, *6*, 1–11. https://doi.org/10.1186/s41601-021-00194-y.
12. Yang, Z.; Xie, C.; Yin, C. Fault location method for distribution network using an additional inductance strategy. *Electronics* **2024**, *13*, 712. https://doi.org/10.3390/electronics13040712.
13. Naidu, O.; Pradhan, A.K. A traveling wave-based fault location method using unsynchronized current measurements. *IEEE Trans. Power Deliv.* **2019**, *34*, 505–513. https://doi.org/10.1109/TPWRD.2018.2875598.
14. Liang, L.; Zhang, H.; Cao, S.; Zhao, X.; Li, H.; Chen, Z. Fault location method for distribution networks based on multi-head graph attention networks. *Front. Energy Res.* **2024**, *12*, 1395737. https://doi.org/10.3389/fenrg.2024.1395737.
15. Zhang, Y.; Wang, J.; Khodayar, M.E. Graph-based faulted line identification using micro-PMU data in distribution systems. *IEEE Trans. Smart Grid* **2020**, *11*, 3982–3992. https://doi.org/10.1109/TSG.2020.2988349.
16. Zarei, S.F.; Khankalantary, S. Protection of active distribution networks with conventional and inverter-based distributed generators. *Int. J. Electr. Power Energy Syst.* **2021**, *129*, 106746. https://doi.org/10.1016/j.ijepes.2020.106746.
17. Cifuentes, H.A.; Mora-Flórez, J.; Pérez-Londóño, S. Time-domain analysis for fault location in power distribution systems considering the load dynamics. *Electr. Power Syst. Res.* **2017**, *146*, 331–340. https://doi.org/10.1016/j.epsr.2017.01.034.
18. IEEE. IEEE Guide for Determining Fault Location on AC Transmission and Distribution Lines; IEEE Std C37.114-2014; IEEE: New York, NY, USA, 2015. https://doi.org/10.1109/IEEESTD.2015.7024095.
19. Das, R. Determining the Location of Faults in Distribution Systems. Ph.D. Thesis, University of Saskatchewan, Saskatoon, Canada, 1998.
20. Yang, W.J.; Yin, X.; Tao, J. Fault current constrained impedance-based method for high resistance ground fault location in distribution grid. *Electr. Power Syst. Res.* **2024**, *227*, 109998. https://doi.org/10.1016/j.epsr.2023.109998.
21. Grainger, J.J.; Stevenson, W.D. *Power System Analysis*; McGraw-Hill: New York, NY, USA, 1994.
22. Feng, D.; Hongfei, S.; Xiangjun, Z.; Fan, X.; Hang, Z.; Yihan, Z. High impedance fault detection method based on sparsity of traveling wave full waveform energy distribution. In Proceedings of the China International Conference on Electricity Distribution (CICED), Changsha, China, 2022; pp. 1566–1570. https://doi.org/10.1109/CICED56215.2022.9929011.
23. Fortescue, C.L. Method of symmetrical coordinates applied to the solution of polyphase networks. *AIEE Trans.* **1918**, *37*, 1027–1140.
24. Julio, R.C.; Ramos, G.; Celeita, D.F. Fault analysis based on time-domain symmetrical components. In Proceedings of the IEEE/IAS 57th Industrial and Commercial Power Systems Technical Conference (I&CPS), Las Vegas, NV, USA, 2021; pp. 1–5. https://doi.org/10.1109/ICPS51807.2021.9416590.
25. Phadke, A.G.; Thorp, J.S. *Computer Relaying for Power Systems*, 2nd ed.; Wiley: Hoboken, NJ, USA, 2009.
26. McInnes, A.D.; Morrison, I.F. Real time calculation of resistance and reactance for transmission line protection by digital computer. *Electr. Eng. Trans. Inst. Eng. Aust.* **1970**, *EE7*, 16–23.

 doi:10.20944/preprints202605.1201.v1

27. Lehtonen, M.; Hakola, T. *Neutral Earthing and Power System Protection: Earthing Solutions and Protective Relaying in Medium Voltage Distribution Networks*; ABB Transmit: Vaasa, Finland, 1996.
28. Dash, C.S.K.; Behera, A.K.; Ghosh, A. An outliers detection and elimination framework in classification task of data mining. *Decis. Anal. J.* **2023**, *6*, 100164.
29. Vargas, M.C.; Mendes, M.A.; Batista, O.E.; Yang, Y. Investigating small-scale DER impact on fault currents and overcurrent protection coordination in distribution feeders under Brazilian technical standards. *Electricity* **2025**, *6*, 54. https://doi.org/10.3390/electricity6030054.
30. Australian Energy Market Operator (AEMO). *Grid Forming and Grid Following Inverter Fault Current Contribution*; AEMO: Melbourne, Australia, 2025.